ELSEVIER

Contents lists available at ScienceDirect

## Case Studies in Thermal Engineering

journal homepage: www.elsevier.com/locate/csite





# Analysis of irregular heat source/sink of a stagnation-point flow toward a vertical plate induced by spherical hybrid nanofluids

Latifah Falah Alharbi <sup>a,b</sup>, Anuar Ishak <sup>a,\*</sup>, Umair Khan <sup>a,c,d</sup>, Iskandar Waini <sup>e</sup>, Sameh E. Ahmed <sup>f</sup>

- <sup>a</sup> Department of Mathematical Sciences, Faculty of Science and Technology, Universiti Kebangsaan Malaysia, UKM Bangi, 43600, Selangor, Malaysia
- <sup>b</sup> Department of Mathematics, College of Science, Qassim University, Qassim, 52571, Saudi Arabia
- <sup>c</sup> Department of Mathematics, Faculty of Science, Sakarya University, Serdivan, Sakarya, 54050, Turkey
- <sup>d</sup> Department of Mechanics and Mathematics, Western Caspian University, Baku, 1001, Azerbaijan
- <sup>e</sup> Fakulti Teknologi Kejuruteraan Mekanikal dan Pembuatan, Universiti Teknikal Malaysia Melaka, Hang Tuah Jaya, Durian Tunggal, 76100, Melaka. Malaysia
- f Department of Mathematics, Faculty of Science, South Valley University, Qena, 83523, Egypt

#### ARTICLE INFO

Handling Editor: Huihe Qiu

Keywords: Hall effect Heat source/sink Hybrid nanofluids MHD Williamson fluid

#### ABSTRACT

Heat transfer technology is quickly increasing as a result of the demand for well-organised heating and cooling systems (HGS and CGS) in the necessary chemical, automotive, and aerospace sectors. Thus, the current study aims to observe mixed convective flow of a Williamson fluid near the stagnation point in the presence of hybrid nanoparticles (Al $_2$ O $_3$  and Cu) across a vertical flat plate with the Hall effect. The water-based alumina (Al $_2$ O $_3$ ) and copper (Cu) nanoparticles that have been convectively heated are evaluated for their suitability in industry. The primary equations are non-dimensionalized employing the relevant similarity factors before being solved numerically by the bvp4c solver in MATLAB software. We examine the impacts of several pertinent parameters on transverse and axial velocities, drag force, temperature, and heat transfer. In the case of opposing flow, two different outputs are obtained, whereas just one is procured in the case of assisting flow. The impact of Lorentz force can also be used to alter the flow and physical properties of heat transfer.

#### 1. Introduction

The industry has extensively used nanofluids. Nanofluid, which has significantly better molecular mobility than traditionally produced fluids [1], is beneficial in a variety of real-world applications, including porous materials [2,3]. In recent years, it has gained popularity for application in medical encapsulation. The addition of metal oxide or nanoparticles to fluids is a well-known approach for modifying their thermal conductivity and heat transfer. Metals are the most ideal nanoparticles because they correlate better with thermal conductivity than normal fluids [4]. Floating a certain type of nanoparticle in ordinary fluids produces a persistent fluid known as nanofluid. Nanofluids often surpass other commonly used liquids such as oil, water, and ethylene glycol in terms of heat

E-mail addresses: lat.alharbi@qu.edu.sa (L.F. Alharbi), anuar\_mi@ukm.edu.my (A. Ishak), umairkhan@sakarya.edu.tr (U. Khan), iskandarwaini@utem.edu.my (I. Waini), samh.sci.math81@gmail.com (S.E. Ahmed).

https://doi.org/10.1016/j.csite.2024.105551

Received 28 April 2023; Received in revised form 12 November 2024; Accepted 21 November 2024 Available online 22 November 2024

2214-157X/© 2024 The Author(s). Published by Elsevier Ltd. This is an open access article under the CC BY-NC-ND license (http://creativecommons.org/licenses/by-nc-nd/4.0/).

<sup>\*</sup> Corresponding author.

transfer. Nanofluids have sparked widespread interest due to their superior heat transfer capabilities. The most well-known concern with HGSs is the inherent difficulty of heat transmission. Pure fluid is a superior option that is easier to find and less expensive. Water is extensively utilised in industry to distribute nano-liquids due to its poor thermal conductivity (TC), which must be improved if used as a heat exchanger through nanoparticle dispersion [5]. Following Masuda et al. [6] the addition of nanoparticles can alter the temperature and viscosity of regular liquids. Choi and Eastman [7] demonstrated that the TC of the liquid increases dramatically as the nanoparticles in conventional fluids disperse. Beg et al. [8] studied the effects of Dufour and Soret, and reported a non-similar solution for buoyant flow along an angled sheet. They found that the negative inclination of the plate leads the flow of fluid to increase, but a positive inclination of the plate has the opposite effect. Anbuchezhian et al. [9] investigated the influence of temperature stratification on the mobility of a nano-liquid across an extended surface powered by solar light. The inclusion of nanofluids has been found to improve the thermal conductivity and convective heat transfer of regular liquids. Khan et al. [10] estimated the ramifications of crucial 3D flow across an exponentially bi-directional stretching surface filled with nanofluid. Zeeshan and Majeed [11] investigated buoyant flow in a porous, non-Darcy environment using stretching surfaces and magnetized ferroparticles. They concluded that, while temperature has the opposite effect, a stronger electric field leads a frictional resistance of the Lorentz force to decline. Shamshuddin et al. [12] developed a model for free convection flow of a magnetized reactive nanofluid across an exponentially stretchable Riga plate induced by double stratification. They observed that the heat transport is reduced across the boundary layer domain with higher Grashof numbers. Recently, Shamshuddin et al. [13] investigated the radiative flow of ethylene-glycol solvent base nanofluids through a permeable cylindrical annulus with irregular viscosity and Soret number. It was observed that momentum shrinks down with increase in the magnetic and Darcy terms.

In recent years, a novel type of nanofluid known as hybrid nanofluids has been studied to improve the heat transmission rate. Hybrid nanofluids are improved nanofluids made up of two distinct nanoparticles, as opposed to standard nanofluids, which only have one type of nanoparticle suspended in the base fluid. Better thermophysical properties given by hybrid nanofluids result in higher heat transfer performance. Devi and Devi [14,15] investigated the flow of hybrid nanofluids on an expanded surface while accounting for Cu-Al<sub>2</sub>O<sub>3</sub> nanoparticles with and without magnetic effects. They discovered that hybrid nanofluids outperform regular nanofluids in terms of heat transfer. Waini et al. [16] investigated the impact of convective boundary conditions using hybrid nanofluids over a stretching/shrinking sheets with suction effect, and reported dual solutions. Salehi et al. [17] investigated magnetic flow through hybrid nanofluids in an ongoing horizontal channel. The velocity distribution was lowered by increasing the Hartman number as well as the squeeze number. Hosseinzadeh et al. [18] studied the flow of a micropolar fluid with hybrid nanoparticles over an upward plate. Their findings showed that for water-based fluids, lamina-shaped nanoparticles have a 38.09 % greater temperature profile than brick-shaped nanoparticles. Gowda et al. [19] examined the flow by distributing ferrite hybrid nanoparticles via a revolving disk that contracts and expands. Shahzad et al. [20] explored the significance of solar collector through nanofluid by incorporating Oldroyd-B fluid in a Darcy-Forchheimer porous medium with radiation effect. They found that the rate of heat transmission in solar power ship increases with a positive shift in the impacts of viscid dissipative, thermal radiation, and suction flow. A source/sink-equipped heated convective surface was recently examined by Animasaun et al. [21] to determine the effects of the magneto effect induced by three different types of nanofluids. The distribution of temperature can be made better by an increase in the convective wall heating. Shamshuddin et al. [22] analyzed the unsteady flow of engine-oil based MoS<sub>2</sub> nanofluid with Hall generator and heat source. They found that the temperature decreases with a growing Prandtl number, whereas temperature increases with higher radiative parameters, nanoparticle volume fractions, and heat source parameters. The impact of entropy generation on the rotating flow of hybrid nanofluid induced by tangent hyperbolic fluid through stretching rotatable sheet was inspected by Shamshuddin et al. [23]. They observed that the thermal conductivity of a hybrid nanofluid is superior to that of a mono disperse nanofluid. Recently, Shamshuddin et al. [24] developed a two-phase model of Casson nanofluid flow via a bi-directional stretchable sheet using unique two-sided reactions. The results show that the higher stretching parameter enhances nanofluid dispersion while reducing Casson parameter towards horizontal velocity in the x and y directions.

The exploration of the dynamics of shear-thinning (pseudoplastic) fluids is gaining popularity because of its importance in biosciences, engineering, and industry. These include sheets composed of extrusion polymers, natural substances with a high melt, and sheets wrapped in photographic film-like emulsions. Several models have been developed to investigate the rheological characteristics of various pseudoplastic fluids (honey, paints, blood, etc.). Some of them are the Cross model, Ellis model, Power-law model, Carreau model, and Williamson fluid model (WFM). We have included the WFM in this research for additional investigation. This model has the benefit of providing both lowest (zero shear stress) and highest (infinite shear stress) viscosities. In 1929, Williamson [25] studied and provided experimental evidence for a particular model to investigate the tendency of pseudoplastic flows. He discussed the relevance of STFs and how they vary from viscous flows. Nadeem et al. [26] revealed that increasing the Williamson factor reduces the friction factor and velocity of the Williamson liquid on a stretching surface. Hayat et al. [27] examined Williamson fluid as it travelled through a stretching sheet, and discovered that the presence of Lorentz forces and heat radiation caused the wall shear stress to decrease faster for greater volumes of Williamson fluid. Shawky et al. [28] investigated the heat and mass transmission properties of Williamson fluid on a permeable stretching surface with magnetic effect. As the permeability and Williamson factors increase, the rate at which heat is transferred to the stretchable sheet accelerates. Yahya et al. [29] investigated the fluid and heat transfer processes through a stretchable sheet in a porous medium. The increased magnetic field and permeability factor are expected to slow the flow rate. Hussain [30] recently investigated the radiative unsteady flow and heat transmission of Williamson fluid with hybrid nanoparticles across a flexible heated surface generated by the slip effect. The HT rate is increased due to the concentration of nanoparticles.

Mixed convection or buoyant flow is employed in a variety of technical applications. Transportation systems that use both free and forced convective flow include solar cells, semiconductors, boilers, and nuclear reactors. When the pressure hydrostatically induced through the temperature gradient bordered by the hard compact surface and the free-stream grows, a mixed convective flow is

necessary, which has a substantial impact on both flow dynamics and thermal HT. Ramachandran et al. [31] scrutinized the 2D buoyant flow through an upright sheet with arbitrary high wall temperatures and variations in surface heat flux. Multiple findings were seen in that zone of flow for a certain range of buoyancy parameters, and their solutions revealed that an area of downward flow was planned for opposing flow conditions. Devi et al. [32] explored unsteady flow in which the time-dependent free-stream velocity accentuates the temperature-flow difference. Ishak et al. [33] studied the flow approaching a stagnation point and heat transmission via a permeable plate under buoyant effect. It was shown that there were two different solutions for buoyant aiding flow, as contrast to the commonly revealed solutions for adverse flow. Ahmad et al. [34] investigated the buoyancy effects of a curved sheet using a catalytic exothermic chemical reaction. They observed that the velocity profile becomes progressively substantial, and the temperature and concentration profiles are evenly distributed due to uniform heating for *n* equal to 1.

MHD is a critical field of engineering and technology. When we think about MHD, two prominent authors spring to mind: Alfven [35] and Cowling [36]. Cowling studied whether Ohm's law should be modified to include Hall currents when sufficiently powerful magnetic fields are applied. If there is a strong magnetic field and a low electron density, the phenomenon of the Hall effect cannot be ignored. Such a strong magnetic orientation is favourable for changing the form of an ionised liquid's movement. The Hall phenomenon is created by additional potential fluctuations on opposite sides of a conductor. As a result, it is determined that electrons, not ions, are accountable for the current's dispersion within the fluid. Many astrophysical instruments rely on the Hall characteristic, including the formation of dense molecular clouds and white dwarfs. Prasad et al. [37] investigated the Hall features of a stream running across a surface of varied thickness. Gandluru et al. [38] reported the oscillating flow of a radiative nanofluid using the Hall effect over a spinning permeable surface. They investigated the Hall factor for speed enhancement. Mabood et al. [39] performed an excellent hydromagnetic investigation of a nanofluid stream running through a rotating channel. They discussed the perception of Hall current and the various viscosity effects on the HT and MT phenomenon. The findings revealed that the spinning component reduced main flow while increasing secondary profile. References [40–45] provide additional information on the importance of MHD and Hall current.

This novelty of the work stems from its objective to investigate the interactions between MHD and Hall consequences on the SPF of Williamson fluid created by hybrid nanofluids across a heated vertical flat plate with uneven heat source or sink and buoyancy effects. In addition, the impacts of thermal radiation and the convective boundary conditions is also examined. The present challenge considers hybrid nanofluids, which are mixtures of two dissimilar nanoparticles (copper and  $Al_2O_3$ ) and a standard base fluid. The similarity technique is used to turn PDEs into nonlinear ODEs, which are then solved with the help of bvp4c solver. Stability analysis is also provided for verifying the physical solution. One of the goals of this research is to calculate a range of results for the opposing flow scenario. The data available shows that no one has yet considered this particular topic.

#### 2. Mathematical formulation of the problem

Consider a mixed convective MHD flow of a Williamson fluid driven by spherical hybrid nanofluids via an upward flat plate with an uneven heat source/sink and Hall current effects. In addition, the behaviours of the convective boundary condition and thermal radiation are also considered. Fig. 1 depicts the flow problem of hybrid nanofluids schematically, with positive  $x_a$ — and  $y_a$ — coordinates determined along the respective surface and upright to the flat plate, and axis coordinates transverse to the plane. The corresponding  $y_a$ — direction exhibits a large external magnetic impact  $B_0$ . The induced magnetic influence is also neglected due to the extremely low attractive Reynolds number. Because electron-atom collisions are thought to be highly powerful, the proposed Hall effect cannot be ignored [46]. Once the Hall current strengthens along the appropriate  $z_a$ — axis, a cross flow occurs, resulting in a 3D flow. We avoided this difficulty by presuming that the flow quantity in the  $z_a$ — direction is constant. This is only true if the length of the flat plate is infinite in that direction. In keeping with the generalized Ohms' law [47], the plate is indeed supposed to be electrically non-conducting and with the intent of  $J_{y_a} = 0$  is pertained consistently past the flow. Considering the presumptions [48,49], the leading equations for regulating the considered flow are supplied, together with Boussinesq approximations are stated as:

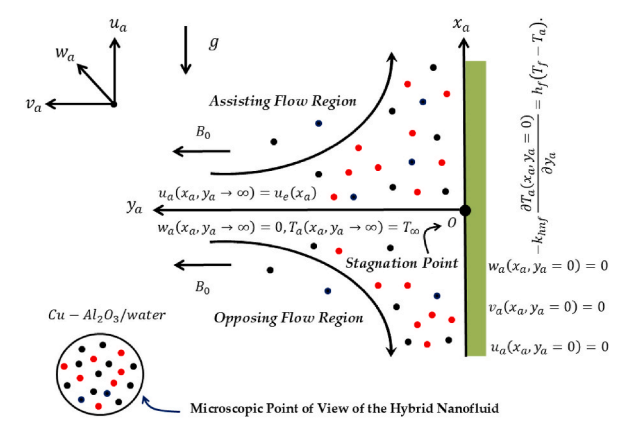


Fig. 1. The physical model of the problem.

$$\frac{\partial u_a}{\partial r_a} + \frac{\partial v_a}{\partial v_a} = 0,\tag{1}$$

$$\begin{split} u_{a}\frac{\partial u_{a}}{\partial x_{a}} + v_{a}\frac{\partial u_{a}}{\partial y_{a}} &= -\frac{1}{\rho_{hnf}}\frac{\partial p_{a}}{\partial x_{a}} + \frac{\mu_{hnf}}{\rho_{hnf}}\left(\frac{\partial^{2}u_{a}}{\partial y_{a}^{2}} + \sqrt{2}\,\Gamma_{a}\frac{\partial^{2}u_{a}}{\partial y_{a}^{2}}\,\frac{\partial u_{a}}{\partial y_{a}}\right) \\ &- \frac{\sigma_{hnf}B_{0}^{2}}{\rho_{hnf}\left(1 + m_{a}^{2}\right)}\left(u_{a} + m_{a}w_{a}\right) + \frac{(\rho\beta)_{hnf}}{\rho_{hnf}}g(T_{a} - T_{\infty}), \end{split} \tag{2}$$

$$u_{a}\frac{\partial w_{a}}{\partial x_{a}} + v_{a}\frac{\partial w_{a}}{\partial y_{a}} = \frac{\mu_{hnf}}{\rho_{hnf}} \left( \frac{\partial^{2} w_{a}}{\partial y_{a}^{2}} + \sqrt{2} \Gamma_{a} \frac{\partial^{2} w_{a}}{\partial y_{a}^{2}} \frac{\partial w_{a}}{\partial y_{a}} \right) + \frac{\sigma_{hnf}B_{0}^{2}}{\rho_{hnf}(1 + m_{a}^{2})} (m_{a}u_{a} - w_{a}), \tag{3}$$

$$u_{a}\frac{\partial T_{a}}{\partial x_{a}} + v_{a}\frac{\partial T_{a}}{\partial y_{a}} = \frac{k_{hnf}}{(\rho c_{p})_{hnf}} \frac{\partial^{2} T_{a}}{\partial y_{a}^{2}} - \frac{1}{(\rho c_{p})_{hnf}} \frac{\partial q_{rad}}{\partial y_{a}} + \frac{1}{(\rho c_{p})_{hnf}} Q^{bbb}, \tag{4}$$

with boundary conditions (BCs) are

$$u_a = 0, v_a = 0, w_a = 0, -k_{lnf} \frac{\partial T_a}{\partial y_a} = h_f (T_f - T_a); T_f = T_\infty + T_A x_a \text{ at } y_a = 0,$$

$$u_a \rightarrow u_e = A x_a, w_a \rightarrow 0, T_a \rightarrow T_\infty \text{ as } y_a \rightarrow \infty.$$
(5)

Here,  $u_a, w_a, v_a$  are the components velocity in the directions of  $x_a-,z_a-$  and  $y_a-$  axes, respectively,  $m_a$  the Hall parameter,  $m_a$  the constant reference temperature,  $\Gamma_a$  the time constant,  $\mu_{hnf}$  the HNF viscosity,  $\rho_{hnf}$  the HNF density,  $T_\infty$  and  $T_a$  indicate the free-stream temperature and the temperature of the HNF, respectively,  $Q^{bbb}$  the irregular heat source/sink,  $q_{rad}$  is the radiative heat flux,  $h_f$  the heat transfer coefficient,  $\sigma_{hnf}$  the EC of the HNF,  $k_{hnf}$  HNF thermal conductivity, g the acceleration due to gravity, and  $(\rho c_p)_{hnf}$  the heat capacity of the HNF. The expression of the HNF is verified as [50]:

$$\frac{\mu_{hnf}}{\mu_f} = \frac{1}{\left(1 - \varphi_{Cu} - \varphi_{Al_2O_3}\right)^{2.5}},\tag{6}$$

$$\frac{\rho_{hnf}}{\rho_f} = \varphi_{Cu} \left( \frac{\rho_{Cu}}{\rho_f} \right) + \varphi_{Al_2O_3} \left( \frac{\rho_{Al_2O_3}}{\rho_f} \right) + \left( 1 - \varphi_{Cu} - \varphi_{Al_2O_3} \right), \tag{7}$$

$$\frac{k_{hnf}}{k_{f}} = \frac{\left[\frac{(\varphi_{Cl}k_{Cl} + \varphi_{Al_{2}O_{3}}k_{Al_{2}O_{3}})}{\varphi_{Cl} + \varphi_{Al_{2}O_{3}}k_{Al_{2}O_{3}}} + \left\{\frac{2k_{f} + 2(\varphi_{Cl}k_{Cl} + \varphi_{Al_{2}O_{3}}k_{Al_{2}O_{3}})}{-2(\varphi_{Cl} + \varphi_{Al_{2}O_{3}})k_{f}}\right\}\right]}{\left[\frac{(\varphi_{Cl}k_{Cl} + \varphi_{Al_{2}O_{3}}k_{Al_{2}O_{3}})}{\varphi_{Cl} + \varphi_{Al_{2}O_{3}}k_{Al_{2}O_{3}}} + \left\{\frac{2k_{f} - (\varphi_{Cl}k_{Cl} + \varphi_{Al_{2}O_{3}}k_{Al_{2}O_{3}})}{+(\varphi_{Cl} + \varphi_{Al_{2}O_{3}})k_{f}}\right\}\right]}, \tag{8}$$

$$\frac{(\rho\beta)_{hnf}}{(\rho\beta)_f} = \varphi_{Cu} \left( \frac{(\rho\beta)_{Cu}}{(\rho\beta)_f} \right) + \varphi_{Al_2O_3} \left( \frac{(\rho\beta)_{Al_2O_3}}{(\rho\beta)_f} \right) + \left( 1 - \varphi_{Cu} - \varphi_{Al_2O_3} \right), \tag{9}$$

$$\frac{\sigma_{hnf}}{\sigma_{f}} = \frac{\left[\frac{\left(\varphi_{Cu}\sigma_{Cu} + \varphi_{Al_{2}O_{3}}\sigma_{Al_{2}O_{3}}\right)}{\varphi_{Cu} + \varphi_{Al_{2}O_{3}}\sigma_{Al_{2}O_{3}}\right) + \left\{ \frac{2\sigma_{f} + 2\left(\varphi_{Cu}\sigma_{Cu} + \varphi_{Al_{2}O_{3}}\sigma_{Al_{2}O_{3}}\right)\right\}}{-2\left(\varphi_{Cu} + \varphi_{Al_{2}O_{3}}\right)\sigma_{f}} \\
\left[\frac{\left(\varphi_{Cu}\sigma_{Cu} + \varphi_{Al_{2}O_{3}}\sigma_{Al_{2}O_{3}}\right)}{\varphi_{Cu} + \varphi_{Al_{2}O_{3}}\sigma_{Al_{2}O_{3}}\right) + \left\{ \frac{2\sigma_{f} - \left(\varphi_{Cu}\sigma_{Cu} + \varphi_{Al_{2}O_{3}}\sigma_{Al_{2}O_{3}}\right)}{+\left(\varphi_{Cu} + \varphi_{Al_{2}O_{3}}\right)\sigma_{f}} \right\}\right],$$
(10)

$$\frac{(\rho c_p)_{hnf}}{(\rho c_p)_f} = \varphi_{Cu} \left( \frac{(\rho c_p)_{Cu}}{(\rho c_p)_f} \right) + \varphi_{Al_2O_3} \left( \frac{(\rho c_p)_{Al_2O_3}}{(\rho c_p)_f} \right) + \left( 1 - \varphi_{Cu} - \varphi_{Al_2O_3} \right). \tag{11}$$

Thus, the above equations (6)–(11) exemplify the physical features of the Cu-Al $_2$ O $_3$ /water hybrid nanofluids wherein  $\varphi$  indicates

Table 1 Thermophysical features of the  $Cu-Al_2O_3/H_2O$  hybrid nanofluids [15,51].

Physical Characteristics	Water	Cu	$Al_2O_3$
$c_p(J/kgK)$	4179	385	765
$\beta \times 10^{-5} (1/K)$	21	1.67	0.85
$\sigma(\Omega/m)^{-1}$	0.05	$5.96  imes 10^7$	$3.5  imes 10^7$
k(W/mK)	0.613	400	40
$\rho(kg/m^3)$	997.1	8933	3970
Pr	6.2	_	-

the solid nanoparticles volume fraction ( $\varphi=0$ ,  $\varphi_{Cu}$  and  $\varphi_{Al_2O_3}$  signify the regular fluid, the copper nanoparticle, and the alumina nanoparticle, respectively). In contrast, the subsequent electrical conductivities of regular liquid and hybrid nanofluid can be characterized as  $\sigma_f$ ,  $\sigma_{Al_2O_3}$  and  $\sigma_{Cu}$ , respectively. The regular fluid and HNF densities are signified, respectively as  $\rho_{Al_2O_3}$ ,  $\rho_{Cu}$  and  $\rho_f$ . The TCNs of the HNF and regular base fluid are suggested, respectively, as  $k_{Al_2O_3}$ ,  $k_{Cu}$  and  $k_f$ . Moreover,  $(\rho\beta)_{Al_2O_3}$ ,  $(\rho\beta)_{Cu}$  and  $(\rho\beta)_f$  are the coefficients of thermal expansion of the hybrid nanofluid and regular base fluid, respectively, and  $(\rho c_p)_{Al_2O_3}$ ,  $(\rho c_p)_{Cu}$  and  $(\rho c_p)_f$  correspond the specific heat capacities of the HNF and regular fluid, respectively. Table 1 provides the experimental data of the copper (Cu) and alumina (Al<sub>2</sub>O<sub>3</sub>) hybrid nanomaterials along with the regular (viscous) fluid.

Moreover, the term of the irregular heat sink or source in above Eq. (4) is symbolized by Q<sup>bbb</sup> and acknowledged as:

$$Q^{bbb} = \frac{k_{hnf}u_e(x_a)}{x_a v_{hnf}} \left[ A_b^* (T_f - T_\infty) e^{-\xi} + B_b^* (T_a - T_\infty) \right], \tag{12}$$

where  $A_b^*$  and  $B_b^*$  communicate the coefficient of exponentially decaying space and the temperature-dependent heat sink or source, respectively. In addition,  $A_b^*$  and  $B_b^*$  suggest negative and positive values which indicate the heat sink and heat source factors. Therefore, the radiative heat flux  $q_{rad}$  is mathematically defined as:

$$q_{rad} = -\frac{4\sigma^*}{3k^*} \frac{\partial T_a^4}{\partial y_a} = -\frac{16\sigma^*}{3k^*} T_\infty^3 \frac{\partial T_a}{\partial y_a}, T_a^4 \approx 4T_a T_\infty^3 - 3T_\infty^4, \tag{13}$$

where  $\sigma^*$  and  $k^*$  illustrate the Stefan-Boltzmann constant and the absorption coefficient, respectively. Thus, inserting equations (12) and (13) into equation (4), the following equation is obtained as:

$$u_{a}\frac{\partial T_{a}}{\partial x_{a}} + v_{a}\frac{\partial T_{a}}{\partial y_{a}} = \frac{k_{f}}{(\rho c_{p})_{hnf}} \left(\frac{k_{hnf}}{k_{f}} + \frac{4}{3}R_{ad}\right) \frac{\partial^{2} T_{a}}{\partial y_{a}^{2}} + \frac{1}{(\rho c_{p})_{hnf}} \frac{k_{hnf}u_{e}(x_{a})}{x_{a}\nu_{hnf}} \left[A_{b}^{*}(T_{f} - T_{\infty})e^{-\xi} + B_{b}^{*}(T_{a} - T_{\infty})\right],$$

$$(14)$$

where  $R_{ad}=rac{4\sigma^*T_{\infty}^3}{k^*k_f}$  is the radiation parameter.

The subsequent self-similarity variant is included in order to simplify the study of the provided flow problem [41,47]:

$$\psi(x_a, y_a) = \sqrt{Av_f} x_a F(\xi), \xi = y_a \sqrt{\frac{A}{v_f}}, w_a = Ax_a G(\xi), S(\xi) = \frac{T_a - T_{\infty}}{T_A x_a},$$
(15)

where  $\psi$  corresponds to the posited 'stream function' and it is differentiated as:  $u_a = \partial \psi / \partial y_a$  and  $v_a = -\partial \psi / \partial x_a$ . Also, Eqs. (2), (3) and (14) generate the subsequent non-linear ODEs with the help of equation (15) as follows:

$$\frac{\mu_{hnf}/\mu_{f}}{\rho_{hnf}/\rho_{f}}F'''(1+We_{b}F'') + FF'' - F^{2} + 1 + \frac{\sigma_{hnf}/\sigma_{f}}{\rho_{hnf}/\rho_{f}} \frac{\Sigma_{b}}{(1+m_{a}^{2})} (1-F'-m_{a}G) + \frac{(\rho\beta)_{hnf}/(\rho\beta)_{f}}{\rho_{hnf}/\rho_{f}} \gamma_{b}S = 0,$$
(16)

$$\frac{\mu_{hnf} / \mu_f}{\rho_{hnf} / \rho_f} G''(1 + We_b G') + FG' - GF' + \frac{\sigma_{hnf} / \sigma_f}{\rho_{hnf} / \rho_f} \frac{\Sigma_b}{(1 + m_a^2)} (m_a F' - G) = 0, \tag{17}$$

$$\left(\frac{k_{hnf}}{k_{f}} + \frac{4}{3}R_{ad}\right)S'' + \Pr\left(\frac{\left(\rho c_{p}\right)_{hnf}}{\left(\rho c_{p}\right)_{f}}\left(FS' - F'S\right) + \frac{\left(k_{hnf}/k_{f}\right)\left(\rho_{hnf}/\rho_{f}\right)}{\mu_{hnf}/\mu_{f}}\left(A_{b}^{*}e^{-\xi} + B_{b}^{*}S\right) = 0,$$

$$(18)$$

subjected to BCs:

$$F(0) = 0, F'(0) = 0, G(0) = 0, \frac{k_{hnf}}{k_f}S'(0) = -Bi_b(1 - S(0)),$$

$$F'(\xi) \to 1, G(\xi) \to 0, S(\xi) \to 0, \text{ at } \xi \to \infty.$$
(19)

Primes (′) indicate differentiation with respect to  $\xi$ . The similarity equations discussed above also included other influential governing constraints such as:  $\Sigma_b = \sigma_f B_0^2 / A \rho_f$ ,  $\gamma_b = g \beta_f B / A^2 = \frac{G r_{\chi_a}}{R c_{\chi_a}^2}$ ,  $G r_{\chi_a} = \frac{g \beta_f (T_f - T_{cs}) x_a^3}{v_f^2}$ ,  $B i_b = h_f \sqrt{v_f / A} / k_f$ ,  $Re_{\chi_a} = \frac{u_e \chi_a}{v_f}$ ,  $Pr = \mu_f c_p / k_f$ , and  $We_b = \sqrt{2} A \Gamma_a \sqrt{Re_{\chi_a}}$  involve the magnetic factor, the buoyancy factor (ratio of Grashof number to the Reynolds number), the convective parameter, the Prandtl number and the Weissenberg constraint, respectively.

The major physical qualities under consideration are the coefficients of skin friction in the transverse and axial directions, as well as heat transmission, which are represented in the following manner [48].

$$C_{fz_a} = \frac{m_w}{\rho_c u_c^2}, C_{fx_a} = \frac{\tau_w}{\rho_c u_c^2}, Nu_{x_a} = \frac{q_w}{k_c T_A},$$
 (20)

where  $m_w$  and  $\tau_w$  are the STs for the WFM unified by hybrid nanofluids, respectively. In addition,  $q_w$  is the corresponding heat defined as:

$$\tau_{w} = \mu_{hnf} \left[ \frac{\partial u_{a}}{\partial y_{a}} + \frac{\Gamma_{a}}{\sqrt{2}} \left( \frac{\partial u_{a}}{\partial y_{a}} \right)^{2} \right]_{y_{a}=0}, m_{w} = \mu_{hnf} \left[ \frac{\partial w_{a}}{\partial y_{a}} + \frac{\Gamma_{a}}{\sqrt{2}} \left( \frac{\partial w_{a}}{\partial y_{a}} \right)^{2} \right]_{y_{a}=0}, \text{ and }$$

$$q_{w} = -k_{hnf} \left( \frac{\partial T_{a}}{\partial y_{a}} \right)_{w} + (q_{rad})_{w}.$$
(21)

Using (15), we get

$$C_{fx_a} Re_{x_a}^{1/2} = \frac{\mu_{hnf}}{\mu_f} \left[ F''(0) + \frac{We_b}{2} (F''(0))^2 \right], C_{fz_a} Re_{x_a}^{1/2} = \frac{\mu_{hnf}}{\mu_f} \left[ G'(0) + \frac{We_b}{2} (G'(0))^2 \right],$$

$$Nu_{x_a} Re_{x_a}^{-1/2} = -\left( \frac{k_{hnf}}{k_f} + \frac{4}{3} R_{ad} \right) S'(0),$$
(22)

where  $Re_{x_a}$  is the local Reynolds number.

#### 3. Stability analysis

In this section, we investigate the temporal stability of two (stable and unstable) solutions branch as time progresses. Merkin [52] was the first to present the analysis of this approach, which was subsequently adopted by Weidman et al. [53]. For the observed working technique, we begin with the new factors as follows:

$$\xi = y_a \sqrt{\frac{A}{v_f}}, u_a = Ax_a \frac{\partial F(\xi, \tau_a)}{\partial \xi}, w_a = Ax_a G(\xi, \tau_a),$$

$$S(\xi, \tau_a) = \frac{T_a - T_\infty}{T_f - T_\infty}, v_a = -\sqrt{Av_f} F(\xi, \tau_a),$$
(23)

where  $\tau_a = At$  signifies the new dimensionless time factor. Furthermore, executing the foregoing equation (23) into the time-dependent version of the required governing equations (2)–(5), which can take the form of:

$$\frac{\mu_{hnf}/\mu_{f}}{\rho_{hnf}/\rho_{f}} \frac{\partial^{3}F}{\partial\xi^{3}} \left(1 + We_{b} \frac{\partial^{2}F}{\partial\xi^{2}}\right) + F \frac{\partial^{2}F}{\partial\xi^{2}} - \left(\frac{\partial F}{\partial\xi}\right)^{2} + \frac{\sigma_{hnf}/\sigma_{f}}{\rho_{hnf}/\rho_{f}} \frac{\Sigma_{b}}{(1 + m_{a}^{2})} \left(1 - \frac{\partial F}{\partial\xi} - m_{a}G\right) + 1 + \frac{(\rho\beta)_{hnf}/(\rho\beta)_{f}}{\rho_{hnf}/\rho_{f}} \gamma_{b}S - \frac{\partial^{2}f}{\partial\xi\partial\tau_{a}} = 0,$$
(24)

$$\frac{\mu_{hnf}/\mu_{f}}{\rho_{hnf}/\rho_{f}} \frac{\partial^{2}G}{\partial\xi^{2}} \left(1 + We_{b} \frac{\partial G}{\partial\xi}\right) + F \frac{\partial G}{\partial\xi} - G \frac{\partial F}{\partial\xi} + \frac{\sigma_{hnf}/\sigma_{f}}{\rho_{hnf}/\rho_{f}} \frac{\Sigma_{b}}{(1 + m_{a}^{2})} \left(m_{a} \frac{\partial F}{\partial\xi} - G\right) - \frac{\partial G}{\partial\tau_{a}} = 0,$$
(25)

$$\left(\frac{k_{hnf}}{k_{f}} + \frac{4}{3}R_{ad}\right)\frac{\partial^{2}S}{\partial\xi^{2}} + \Pr\left(\frac{(\rho c_{p})_{hnf}}{(\rho c_{p})_{f}}\left(F\frac{\partial S}{\partial\xi} - S\frac{\partial F}{\partial\xi}\right) + \frac{(k_{hnf}/k_{f})(\rho_{hnf}/\rho_{f})}{\mu_{hnf}/\mu_{f}}\left(\frac{A_{b}^{*}e^{-\xi} + B_{b}^{*}S}{B_{b}^{*}S}\right) - \frac{\partial S}{\partial\tau_{a}} = 0$$
(26)

subjected to BCs

$$\frac{\partial F(0,\tau_a)}{\partial \xi} = 0, F(0,\tau_a) = 0, G(0,\tau_a) = 0, \frac{k_{hnf}}{k_f} \frac{\partial S(0,\tau_a)}{\partial \xi} = -Bi_b(1 - S(0,\tau_a)),$$

$$\frac{\partial F(\xi,\tau_a)}{\partial \xi} \to 1, G(\xi,\tau_a) \to 0, S(\xi,\tau_a) \to 0, \text{ at } \xi \to \infty.$$
(27)

In references [52,53], the time independent solutions  $F(\xi) = F_0(\xi)$ ,  $G(\xi) = G_0(\xi)$ , and  $G(\xi) = G_0(\xi)$  of the similarity equations (16)—

#### (18) are perturbed as follows:

$$F(\xi, \tau_a) = F_0(\xi) + e^{-\tau_a \delta_b} f(\xi, \tau_a), G(\xi, \tau_a) = G_0(\xi) + e^{-\tau_a \delta_b} g(\xi, \tau_a),$$

$$S(\xi, \tau_a) = S_0(\xi) + e^{-\tau_a \delta_b} s(\xi, \tau_a),$$
(28)

where  $f(\xi, \tau_a)$ ,  $g(\xi, \tau_a)$  and  $s(\xi, \tau_a)$  in Eq. (28) are comparatively small over the functions  $F_0(\xi)$ ,  $G_0(\xi)$  and  $S_0(\xi)$ , respectively. To check the stability, the outcomes are determined by the sign (positive or negative) of the eigenvalue  $\delta_b$ . Hence, by putting,  $\tau_a = 0$ , we have  $f(\xi) = f_0(\xi)$ ,  $g(\xi) = g_0(\xi)$  and  $s(\xi) = s_0(\xi)$ . Moreover, exercising equation (28) into the above equations (24)–(27), the linearized equations are:

$$\frac{\mu_{hnf}/\mu_{f}}{\rho_{hnf}/\rho_{f}}f_{0}^{"'}(1+We_{b}F_{0}^{"}) + \frac{\mu_{hnf}/\mu_{f}}{\rho_{hnf}/\rho_{f}}We_{b}F_{0}^{"'}f_{0}^{"} + F_{0}f_{0}^{"} + F_{0}F_{0}^{"} - 2F_{0}'f_{0}' -$$

$$\frac{\mu_{hnf}/\mu_{f}}{\rho_{hnf}/\rho_{f}} g_{0}^{"}(1 + We_{b}G_{0}^{'}) + \frac{\mu_{hnf}/\mu_{f}}{\rho_{hnf}/\rho_{f}} We_{b}G_{0}^{"}g_{0}^{'} + F_{0}g_{0}^{'} + F_{0}g_{0}^{'} - G_{0}f_{0}^{'} - G_{0}F_{0}^{'} - g_{0}F_{0}^{'} + \frac{\sigma_{hnf}/\sigma_{f}}{\rho_{hnf}/\rho_{f}} \frac{\Sigma_{b}}{(1 + m_{a}^{2})} (m_{a}f_{0}^{'} - g_{0}) + \delta_{b}g_{0} = 0,$$
(30)

$$\frac{\left(\frac{k_{hnf}}{k_{f}} + \frac{4}{3}R_{ad}\right)s_{0}'' + \Pr\left(\frac{(\rho c_{p})_{hnf}}{(\rho c_{p})_{f}}\left(F_{0}s_{0}' + f_{0}S_{0}' - s_{0}F_{0}'\right) + \frac{\left(k_{hnf}/k_{f}\right)\left(\rho_{hnf}/\rho_{f}\right)}{\mu_{hnf}/\mu_{f}}B_{b}^{*}s_{0} + \delta_{b}s_{0} = 0,$$
(31)

along with BCs

$$f_{0}'(0) = 0, f_{0}(0) = 0, g_{0}(0) = 0, \frac{k_{hnf}}{k_{f}} s_{0}'(0) = Bi_{b} s_{0}(0),$$

$$f_{0}'(\xi) \to 0, g_{0}(\xi) \to 0, s_{0}(\xi) \to 0, \text{at } \xi \to \infty.$$
(32)

The corresponding positive or negative values of  $\delta_b$  in the above equations (29)–(32) are found by setting the value of  $f_0''(0)$ ,  $g_0'(0)$  or  $s_0'(0)$ . Without loss of generality, we set  $f_0''(0) = 1$ ; and resolve the set of coupled equations (29)–(32) to find the eigenvalues  $\delta_b$ , see (Harris et al. [54]).

#### 4. Methodology

The bvp4c approach was used to numerically solve the modified system of nonlinear equations (16)–(18) with BCs (19) for various values of the key restrictions involved in the resulting ( $Cu-Al_2O_3$ /water) hybrid nanofluid flow problem. The bvp4c depends on the '3-stage Lobatto IIIA' formula and is carried out using the finite difference method, which is also known as a collocation formula. It produces an interval-based collocation polynomial of fourth-order accuracy that is uniformly distributed along the C1 continuous outcomes. The residual of the continuous solution provides the basis for mesh selection and error control. To begin the process, novel variables are implemented as

$$F = N_1, F' = N_2, F'' = N_3, G = N_4, G' = N_5, S = N_6, S' = N_7.$$
 (33)

To create a collection of first-order ODEs, we must convert the previously described equation (33) into the non-dimensional similarity equations (16)–(19). This generate the following expression:

$$\frac{d}{d\xi} \begin{pmatrix} N_{1} \\ N_{2} \\ N_{3} \\ N_{4} \\ N_{5} \\ N_{6} \\ N_{7} \end{pmatrix} = \begin{pmatrix} N_{2} \\ \frac{\rho_{hnf}/\rho_{f}}{\mu_{hnf}/\mu_{f}(1+We_{b}N_{3})} \begin{pmatrix} N_{3}^{2}-N_{1}N_{3}-1-\\ \frac{\sigma_{hnf}/\sigma_{f}}{\rho_{hnf}/\rho_{f}} & \frac{\Sigma_{b}}{(1-N_{2}-m_{a}N_{4})} \\ -\frac{(\rho\beta)_{hnf}/(\rho\beta)_{f}}{\rho_{hnf}/\rho_{f}} & \gamma_{b}N_{6} \end{pmatrix},$$

$$N_{5} \\ \frac{\rho_{hnf}/\rho_{f}}{\mu_{hnf}/\mu_{f}(1+We_{b}N_{5})} \begin{pmatrix} N_{2}N_{4}-N_{1}N_{5}-\frac{\sigma_{hnf}/\sigma_{f}}{\rho_{hnf}/\rho_{f}} & \frac{\Sigma_{b}}{(1+m_{a}^{2})}(m_{a}N_{2}-N_{4}) \\ N_{7} \end{pmatrix},$$

$$N_{7} \\ \frac{1}{\begin{pmatrix} \frac{K_{hnf}}{k_{f}}+\frac{4}{3}R_{ad} \end{pmatrix}} \begin{pmatrix} -\Pr\frac{(\rho c_{p})_{hnf}}{(\rho c_{p})_{f}} & (N_{1}N_{7}-N_{2}N_{6})-\\ \frac{(K_{hnf}/k_{f})(\rho_{hnf}/\rho_{f})}{\mu_{hnf}/\mu_{f}} & (A_{b}^{*}e^{-\xi}+B_{b}^{*}N_{6}) \end{pmatrix}.$$
The boundary conditions are

The boundary conditions are

$$N_{1}(\xi) = 0, N_{2}(\xi) = 0, N_{4}(\xi) = 0, \frac{k_{hnf}}{k_{f}} N_{7}(\xi) + Bi(1 - N_{6}(\xi)) = 0, \text{ as } \xi = 0$$

$$N_{2}(\xi) \to 1, N_{4}(\xi) \to 0, N_{6}(\xi) \to 0 \text{ at } \xi \to \infty.$$
(35)

In this method, the correctness of the results governs residuality and mesh selection. This methodology is a residual-type method, and its efficiency is determined on the quality of the initial estimates provided, as well as the fulfilment of the stated requirements (35). The mesh size is set to be around 0.01. As a result, length-sized adjustments are used to achieve increased accuracy, which approaches  $10^{-10}$ .

#### 5. Results and discussion

This section examines the numerical outputs in both quantitative and pictorial formats for stable and unstable outcomes. As a result, to comprehend the dual solutions of a limited scenario, it is important to initially examine the technique, code dependability, and results validation.

Table 2 clarifies the assessment of the friction factor and heat transport for the dissimilar amount of  $\Sigma_b$  by published work (Ishak et al. [55]) when  $m_a = 0$ ,  $\varphi_{Cu} = 0$ ,  $u_e(x_a) = 0$ ,  $We_b = 0$ ,  $\varphi_{Al_2O_3} = 0$ , Pr = 1,  $\gamma_b = 1.0$ ,  $A_b^* = 0$ ,  $B_b^* = 0$ ,  $R_{ad} = 0$ , and S(0) = 1. The solutions show that the initial branch solutions are in excellent agreement with Ishak et al. [55]. We believe that the offered code is well-designed to uncover the unknown results of the presented problem, based on the great alignment of the solutions as shown in the

The heat transfer, skin friction, and profiles of the spherical hybrid nanofluid for stable and unstable results are visually presented in multiple images as well as Tables 3-5, allowing you to see how various essential factors affect the friction factor in both directions. In the given study, the simulators were employed to solve the specified problem by altering a single parameter at a time while keeping the others constant. During the simulation, the physical parameter values are fixed as  $\varphi_{Al_2O_3}=0.025, \, \varphi_{Cu}=0.025, \, We_b=0.05, \, \gamma_b=-0.005, \, \gamma_b=-0.$ 3.5,  $\Sigma_b = 0.15$ ,  $m_a = 0.5$ ,  $A_b^*$ ,  $B_b^*$ ,  $R_{ad} = 0.05$ , and  $Bi_b = 1.3$ . In the whole study, the first (stable) and second (unstable) solutions are represented by black solid and dash lines, respectively. The small solid pink, red, and black balls symbolize the critical or bifurcation

Table 2 Comparison of  $C_{fx_a} \operatorname{Re}_{x_a}^{1/2}$  and  $Nu_{x_a} \operatorname{Re}_{x_a}^{-1/2}$  for different  $\Sigma_b$ .

$\Sigma_b$	Ishak et al. [55]		Current outcomes	
	$Nu_{x_a} \operatorname{Re}_{x_a}^{-1/2}$	$C_{fx_a} \mathrm{Re}_{x_a}^{1/2}$	$Nu_{x_a} \operatorname{Re}_{x_a}^{-1/2}$	$C_{fx_a} \operatorname{Re}_{x_a}^{1/2}$
0.00	1.0873	-0.5607	1.087336	-0.560723
0.01	1.0863	-0.5658	1.086323	-0.565813
0.04	1.0833	-0.5810	1.083329	-0.581056
0.25	1.0630	-0.6830	1.063014	-0.683035
1	1.0000	-1.0000	1.000000	-1.000000
4	0.8311	-1.8968	0.831129	-1.896819
25	0.4702	-4.9155	0.470228	-4.915523

**Table 3** Numerical outcomes of  $C_{fx_a} \operatorname{Re}_{x_a}^{1/2}$  for change values of  $\varphi_{Al_2O_3}$ ,  $\varphi_{Cu}$ ,  $\Sigma_b$ ,  $We_b$  and  $m_a$  when  $A_b^* = B_b^* = -0.3$ ,  $Bi_b = 1.5$ ,  $\gamma_b = -7.0$ , and  $R_{ad} = 0.05$ .

Parameters				$C_{fx_a} \operatorname{Re}_{x_a}^{1/2}$	
$\varphi_{Al_2O_3}, \varphi_{Cu}$	$\Sigma_b$	$m_a$	$We_b$	UBS	LBS
0.030	0.04	0.5	0.05	0.4973	-1.0230
0.034	_	_	_	0.5519	-1.0639
0.038	_	_	_	0.6058	-1.1037
0.030	0.04	0.5	0.05	0.4973	-1.0230
_	0.07	_	_	0.5164	-1.0320
_	0.10	_	_	0.5349	-1.0406
0.030	0.04	0.5	0.05	0.4973	-1.0230
_	_	0.6	_	0.4952	-1.0220
_	_	0.7	_	0.4930	-1.0210
0.030	0.04	0.5	0.03	0.4937	-1.0251
_	_	-	0.05	0.4973	-1.0230
_	_		0.07	0.5009	-1.0209

Table 4 Numerical outcomes of  $C_{fz_a} \operatorname{Re}_{x_a}^{1/2}$  for change values of  $\varphi_{Al_2O_3}, \varphi_{Cu}, \Sigma_b$ ,  $We_b$  and  $m_a$  when  $A_b^* = B_b^* = -0.3$ ,  $Bi_b = 1.5$ ,  $\gamma_b = -7$  and  $R_{ad} = 0.05$ .

Parameters			$C_{f\!z_a}\mathrm{Re}_{\chi_a}^{1/2}$		
$\varphi_{Al_2O_3}, \varphi_{Cu}$	$\Sigma_b$	$m_a$	$We_b$	UBS	LBS
0.030	0.04	0.5	0.05	0.0106	0.0048
0.034	_	_	_	0.0108	0.0047
0.038	_	_	_	0.0111	0.0046
0.030	0.04	0.5	0.05	0.0106	0.0048
_	0.07	_	_	0.0183	0.0081
_	0.10	_	_	0.0258	0.0112
0.030	0.04	0.5	0.05	0.0106	0.0048
-	_	0.6	_	0.0117	0.0054
_	_	0.7	_	0.0124	0.0057
0.030	0.04	0.5	0.03	0.0106	0.0048
_	_	-	0.05	0.0105	0.0048
-	-	-	0.07	0.0104	0.0048

Table 5 Numerical outcomes of  $Nu_{x_a} \operatorname{Re}_{x_a}^{-1/2}$  for change values of  $\varphi_{Al_2O_3}$ ,  $\varphi_{Cu}$ ,  $A_b^*$ ,  $B_b^*$  and  $R_{ad}$  when  $\Sigma_b = 0.04$ ,  $m_a = 0.5$ ,  $\gamma_b = -7.0$ ,  $We_b = 0.05$ , and  $Bi_b = 1.5$ .

Parameters		$Nu_{x_a} \mathrm{Re}_{x_a}^{-1/2}$		
$\varphi_{Al_2O_3}, \varphi_{Cu}$	$R_{ad}$	$A_b^*, B_b^*$	UBS	LBS
0.030	0.05	-0.30	0.8868	0.5895
0.034	_	_	0.8976	0.5873
0.038	_	_	0.9080	0.5856
0.030	0.05	-0.30	0.8868	0.5895
_	0.10	_	0.9520	0.6238
_	0.15	_	0.9532	0.6586
0.030	0.05	-0.30	0.8868	0.5895
_	_	-0.32	0.8954	0.5897
_	_	-0.34	0.9038	0.5899
0.030	0.05	0.20	0.8911	0.5607
_	_	0.30	0.8745	0.5606
_	_	0.40	0.8534	0.5605

point, which is where the two solutions intersect.

Tables 3 and 4 display the computable solutions of  $C_{fx_a} Re_{x_a}^{1/2}$  for the first and second solutions with adjustments in  $\varphi_{Al_2O_3}$ ,  $\varphi_{Cu}$ ,  $\Sigma_b$ ,  $We_b$ , and  $m_a$  in both directions. Although the solutions display that for the first solution with complex values of  $\varphi_{Al_2O_3}$ ,  $\varphi_{Cu}$  and  $\Sigma_b$ , in both directions, the shear stress enhances, the same restrictions can alter the mobility of the hybrid nanofluid in the second solution. However, bigger impacts due to the Hall constraint cause the friction factor to grow and fall in both directions. Physically, the Hall effect diminishes useable conductivity, lowering magnetic resonance with both transverse and axial velocity. The friction factor thus rises in the transverse direction. On the other hand, Table 5 shows quantitative estimates for the heat transfer for first and second solutions. With the superior impact of  $\varphi_{Al_2O_3}$ ,  $\varphi_{Cu}$  and  $A_h^*$ ,  $B_h^*$ , the stable branch solution of heat transfer acts brilliantly in this case when

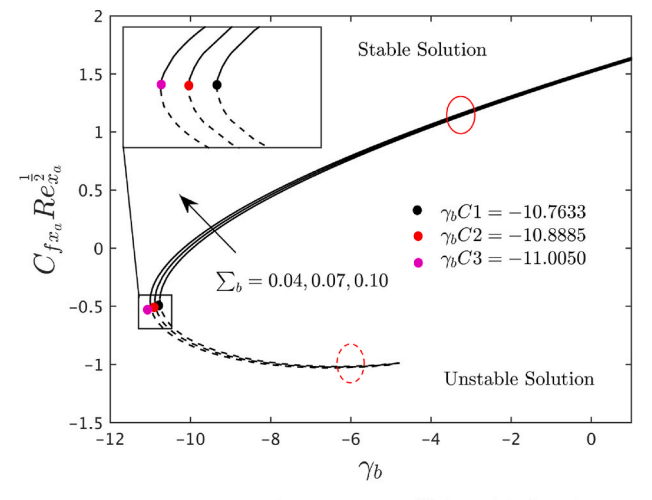
quantitatively matched to the unstable branch solution. Quantitatively, the Nusselt number is increased as  $R_{ad}$  increases in both solutions. Moreover, the dimensionless convective parameter and the heat transfer coefficient are also exactly proportional. Basic physics states that if we increase  $R_{ad}$ , the heat transfer will increase as a result. As a consequence, the Nusselt number will be greatly increased for both solutions.

Fig. 2(a–c) exemplify the discrepancy of magnetic effect  $(\Sigma_b)$  against  $\gamma_b$  on  $C_{fx_a} \operatorname{Re}_{x_a}^{1/2}$ ,  $C_{fz_a} \operatorname{Re}_{z_a}^{1/2}$  and  $Nu_{x_a} \operatorname{Re}_{x_a}^{-1/2}$  of the water-based copper and alumina hybrid nanofluids, respectively. Outcomes exhibit that the friction factor in both directions raise with growing  $\Sigma_h$ for the first solution (see Fig. 2a and b). For the second solution, though, the solution behavior is similar in the transverse directions of friction factor and upturned in the axial direction of the friction factor. In general, a drag kind of force called Lorentz forces tend to reduce flow velocity, which results in a depressed of BLT. Hence, the relationship between the velocity and the coefficient of shear stresses is inversed. The effect of  $\Sigma_h$  leads to uplift the shear stress. Fig. 2c shows that the heat transfer for the first solution falls with increasing  $\Sigma_b$ , while it is higher for the second solution. The Nusselt number and the width of the thermal boundary-layer both grow consequently of the substantial barrier to fluid motion caused by Lorentz forces, that also generates heat. Also, a significant distance from the flat plate causes the fluid's temperature to vanish. This is not unexpected given that the free convective flow is retarded by a magnetic field. Such fluids can have their physical characteristics changed by adjusting the impact of  $\Sigma_h$  parameter. The acquired solution shows that the flow can be controlled by the magnetic field and the properties of HT. Also, the different critical values for each of the chosen default values for  $\Sigma_b$  are determined (see the window of the graphs). With mounting values of  $\Sigma_b$ , the value at the crucial or bifurcation point increases in magnitude. This pattern therefore shows that the liquid flow separation diminishes as the impacts of  $\Sigma_b$  rise. In addition, for negative choice of  $\gamma_b$ , a bifurcation value  $\gamma_b C1$  exists, with double solutions for  $\gamma_b > \gamma_b C1$ , a saddle node bifurcation at  $\gamma_b = \gamma_b C1$  and so outcome for  $\gamma_b < \gamma_b C1$ . The boundary layer separation occurs at  $\gamma_b = \gamma_b C1$ , thus, the solution cannot be found beyond this point.

Fig. 3(a–c) reveal the influence of  $We_b$  on  $C_{fx_a} Re_{x_a}^{1/2}$ ,  $C_{fz_a} Re_{x_a}^{1/2}$  and  $Nu_{x_a} Re_{x_a}^{-1/2}$  for both outcomes. These outcomes express that the values of  $C_{fx_a} Re_{x_a}^{1/2}$ ,  $C_{fz_a} Re_{x_a}^{1/2}$  and  $Nu_{x_a} Re_{x_a}^{-1/2}$  enhance in both outcomes. Additionally, the crucial values show that the Williamson parameter slows boundary layer separation. These images also show that the values of the HT are positive, which indicates that heat is moving from a warm surface to a cool fluid.

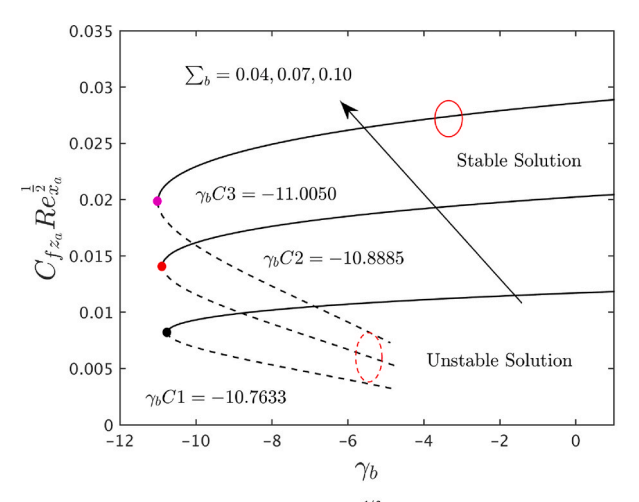
The impact of the convective parameter  $Bi_b$  on  $Nu_{x_a} Re_{x_a}^{-1/2}$  and  $S(\xi)$  of the spherical hybrid nanofluid for both solutions is prostrated in the respective Fig. 4a and b. Fig. 4a divulges that the heat transfer enhances with uplifting values of  $Bi_b$  in both outcomes. Additionally, the strength of the critical values declines as the convective impact increases. This propensity demonstrates that the separation of boundary layer enlarges due to the superior impact of the convective parameter. Fig. 4b suggests that due to enhance in the values of  $Bi_b$ , as a result, the slope of the temperature increases for the first solution, and a small alteration is observed for the second solution. Also, it produces better convective kind of heating of the plate at the wall surface. Now the thermal efficiency can penetrate the static fluid more deeply. Thus, as  $Bi_b$  enhances, likewise, the TBL's thickness and the temperature. It is important to note that for such boundary S(0) = 1 the temperature can be restored by utilizing a convective limitation with a pretty large influence. Also,  $Bi_b = 0$  relates to the insulated case of the sheet.

Fig. 5a, b and 5c exhibit the behavior of  $\varphi_{Al_2O_3}$ ,  $\varphi_{Cu}$  on  $F(\xi)$ ,  $G(\xi)$  and  $S(\xi)$  for the first and second solution, respectively. Results show that  $F'(\xi)$  initially exhibits an intensifying tendency for the first solution before beginning to continuously shrinkage for both branches as a result of the increase in  $\varphi_{Al_2O_3}$ ,  $\varphi_{Cu}$ . Meanwhile, the velocity profile in the transverse direction declines and then inclines for the second solution with superior impacts of  $\varphi_{Al_2O_3}$ ,  $\varphi_{Cu}$  while it is increases continuously for the first solution branch. In addition,



**a.** Impact of  $\Sigma_b$  on  $C_{fk_0}$  Re $_{k_0}^{1/2}$  in axial direction.

**Fig. 2a.** Impact of  $\Sigma_b$  on  $C_{fx_a} \operatorname{Re}_{x_a}^{1/2}$  in axial direction.



**b.** Impact of  $\Sigma_b$  on  $C_{fz_a} \operatorname{Re}_{z_a}^{1/2}$  in the transverse direction.

**Fig. 2b.** Impact of  $\Sigma_b$  on  $C_{fz_a} Re_{z_a}^{1/2}$  in the transverse direction.

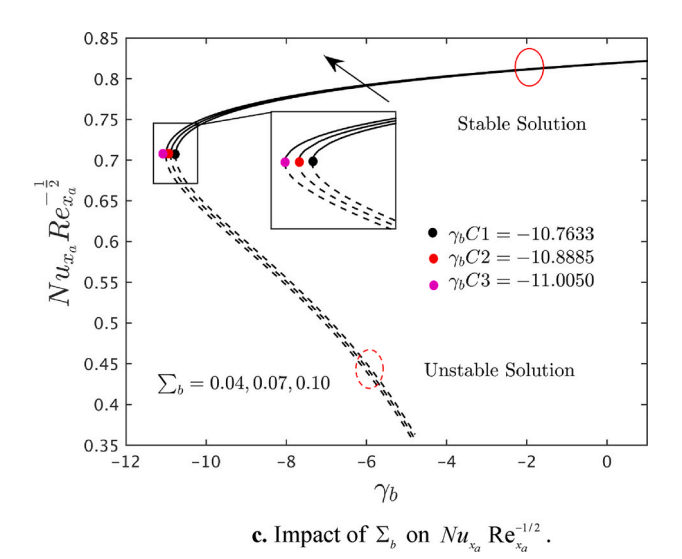


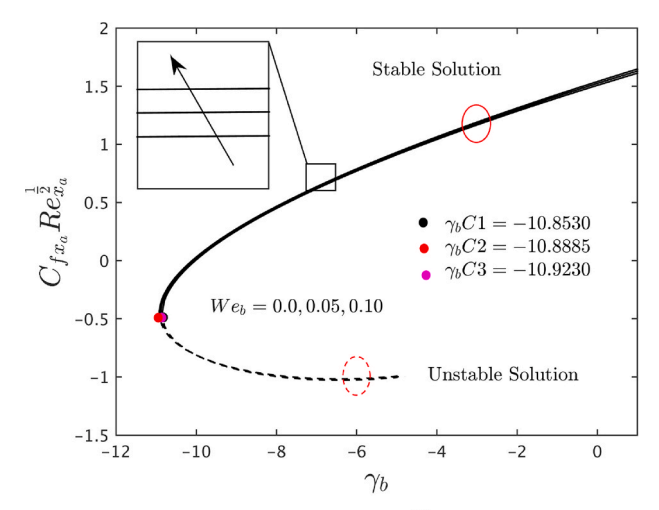
**Fig. 2c.** Impact of  $\Sigma_b$  on  $Nu_{x_a} \operatorname{Re}_{x_a}^{-1/2}$ .

 $S(\xi)$  increases for both solutions with superior impression of  $\varphi_{Al_2O_3}, \varphi_{Cu}$ . Physically, it is important to note that as the volume fraction of nanoparticles grows, so does their heat conductivity. This significantly improves both the temperature profile and the thermal boundary layer.

Fig. 6. Shows the eigenvalues  $\delta_b$  for distinct values of  $\gamma_b$  when  $\mathbf{W}e_b = 0.05$ ,  $m_a = 0.5$ ,  $\Sigma_b = 0.10$ ,  $A_b^* = B_b^* = -0.3$ ,  $R_{ad} = 0.05$ , R

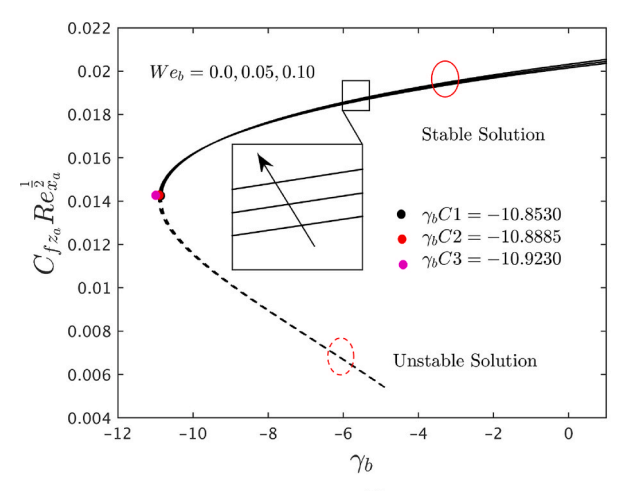
#### 6. Conclusions

The goal of this study is to look at the combined effects of Hall current and MHD on a Williamson fluid containing hybrid nanofluid as it flows over a vertical heated plate with an uneven heat source/sink and radiation effects. The bvp4c solver was applied to numerically solve the resulting ODE system over a wide range of parameter values. We can derive the subsequent findings from this



**a.** Impact of  $We_b$  on  $C_{f_{x_a}} \operatorname{Re}_{x_a}^{1/2}$  in the axial direction.

**Fig. 3a.** Impact of  $We_b$  on  $C_{fx_a}Re_{x_a}^{1/2}$  in the axial direction.

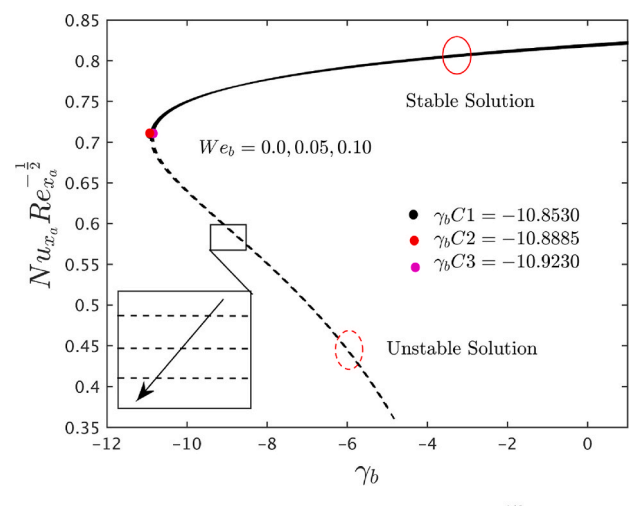


**b.** Impact of  $We_b$  on  $C_{f_{a}} \operatorname{Re}_{z_a}^{1/2}$  in the transverse direction.

**Fig. 3b.** Impact of  $We_b$  on  $C_{fz_a} \operatorname{Re}_{z_a}^{1/2}$  in the transverse direction.

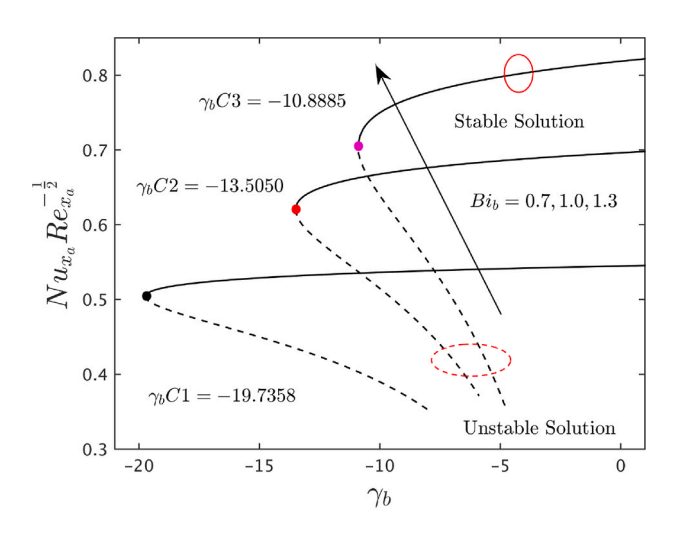
#### research.

- The magnetic number enhances heat transmission and shear stress in the axial direction in the first solution, but has entirely dissimilar impact for the second solution.
- The coefficient of friction factor in the transverse axis increases with the magnetic number for both branches.
- The magnitude of the bifurcation values grows as the magnetic parameter values increase.
- The heat transfer decelerates owing to the higher values of the heat source while it escalates with superior impact of heat sink parameter.
- The shear stress falls in the axial direction due to the increased impact of the Hall parameter, whereas the shear stress increases in the transverse direction.
- The nanoparticles accelerate heat transmission for the first solution while slowing it down for the second.
- The Williamson parameter increases both shear stress and heat transmission.
- According to the temporal stability analysis, the first solution remains physically stable over time, whereas the second solution is unreliable in the long run.



**c.** Impact of  $We_b$  on  $Nu_{x_a} \operatorname{Re}_{x_a}^{-1/2}$ .

**Fig. 3c.** Impact of  $We_b$  on  $Nu_{x_a}Re_{x_a}^{-1/2}$ .



**a.** Impact of  $Bi_b$  on  $Nu_{x_a} \operatorname{Re}^{-1/2}_{x_a}$ .

**Fig. 4a.** Impact of  $Bi_b$  on  $Nu_{x_a}Re_{x_a}^{-1/2}$ .

#### CRediT authorship contribution statement

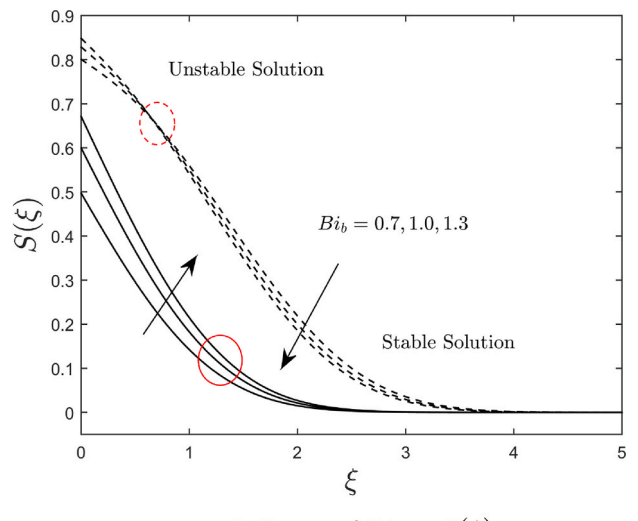
Latifah Falah Alharbi: Conceptualization, Formal analysis, Investigation, Methodology, Software, Validation, Writing – original draft. Anuar Ishak: Funding acquisition, Resources, Supervision, Writing – review & editing. Umair Khan: Methodology, Software, Validation, Writing – review & editing. Iskandar Waini: Methodology, Supervision, Validation, Writing – review & editing. Sameh E. Ahmed: Supervision, Writing – review & editing.

### **Funding**

Universiti Kebangsaan Malaysia (DIP-2023-005)

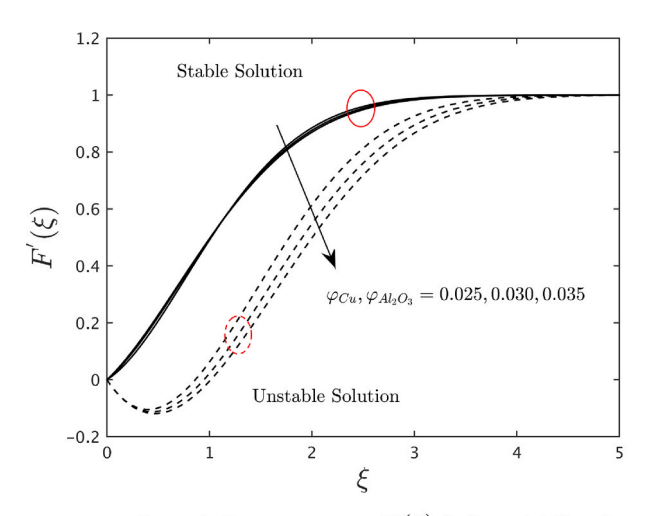
#### Declaration of competing interest

The authors declare that they have no known competing financial interests or personal relationships that could have appeared to influence the work reported in this paper.



**b.** Impact of  $Bi_b$  on  $S(\xi)$ .

**Fig. 4b.** Impact of  $Bi_b$  on  $S(\xi)$ .



**a.** Impact of  $\varphi_{Al_2O_3}$ ,  $\varphi_{Cu}$  on  $F'(\xi)$  in the axial direction.

**Fig. 5a.** Impact of  $\varphi_{Al_2O_3}, \varphi_{Cu}$  on  $F'(\xi)$  in the axial direction.

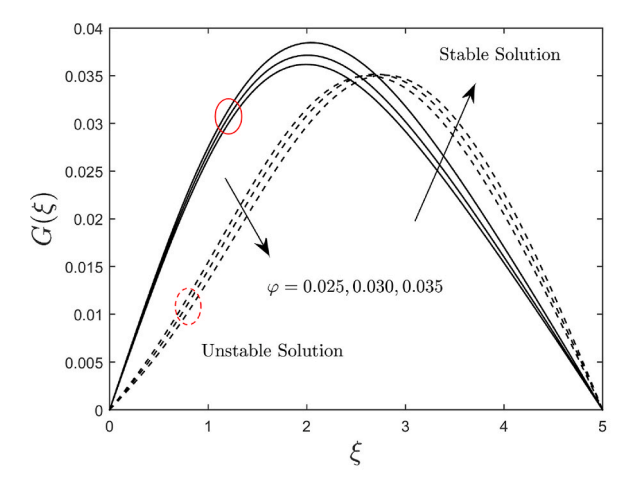
## Nomenclature

$A_b^*$	Coefficient of exponentially decaying space
$B_b^*$	Coefficient of the temperature-dependent heat sink or source
$Bi_b$	Convective parameter
g	Acceleration due to gravity (m/s <sup>2</sup> )
$h_f$	Heat transfer coefficient
$\Sigma_b$	Magnetic factor
$m_a$	Hall parameter
$Q^{bbb}$	Irregular heat source/sink
$q_w$	Heat flux at the wall surface (W/m <sup>2</sup> )
$(x_a,y_a,z_a)$	Cartesian coordinates (m)

 $We_b$  Weissenberg constraint  $T_a$  Temperature (K)

k Thermal conductivity (kg m/s<sup>3</sup> K)

 $(u_a, v_a, w_a)$  Velocity components (m/s)



**b.** Impact of  $\varphi_{Al_2O_3}, \varphi_{Cu}$  on  $G(\xi)$  in the transverse direction.

**Fig. 5b.** Impact of  $\varphi_{Al_2O_3}, \varphi_{Cu}$  on  $G(\xi)$  in the transverse direction.

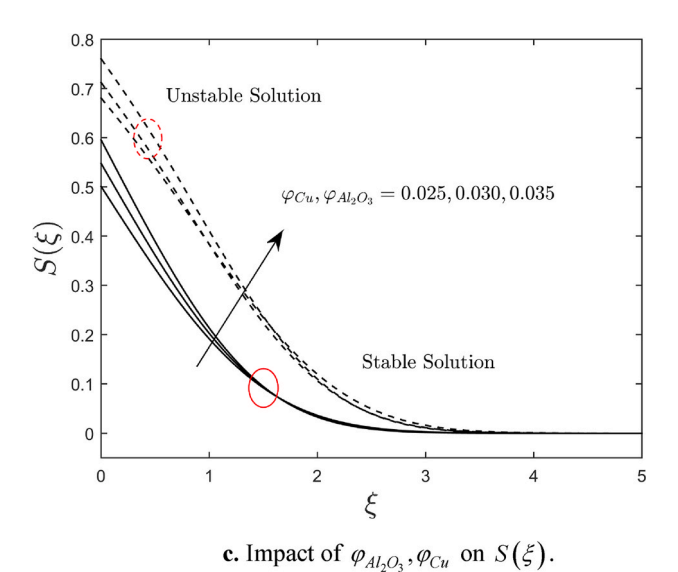


**Fig. 5c.** Impact of  $\varphi_{Al_2O_3}$ ,  $\varphi_{Cu}$  on  $S(\xi)$ .

$k^*$	Boltzmann constant
$T_{\infty}$	Ambient temperature (K)
Pr	Prandtl number
$q_{rad}$	Radiative heat flux (J)
$Re_{x_a}$	Reynolds number

 $F'(\xi)$  Dimensionless velocity in the axial direction  $G(\xi)$  Dimensionless velocity in the transverse direction

 $S(\xi)$  Dimensionless temperature  $C_{fz_a}, C_{fx_a}$  Skin friction coefficients  $Nu_{x_a}$  Local Nusselt number

## Greek symbols

 $\Sigma_b$  Magnetic effect

μ Dynamic viscosity (Kg/m s)

 $\rho$  Density (Kg/m<sup>3</sup>)

 $(\rho c_p)$  Specific heat capacity at constant pressure (m<sup>2</sup>/s<sup>2</sup> K)

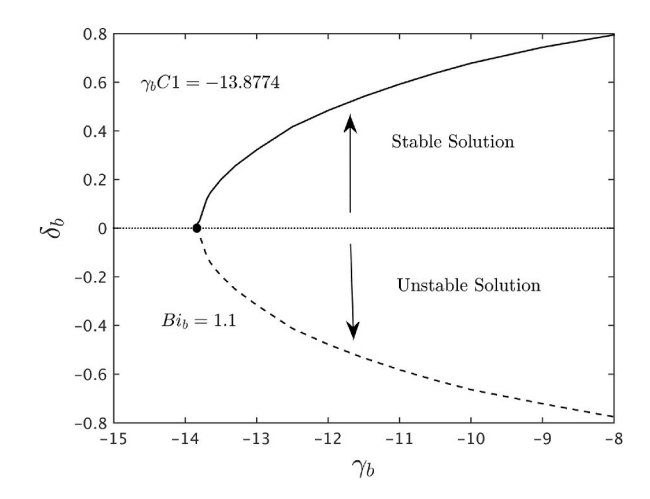


Fig. 6. The smallest eigenvalue  $\delta_b$  for distinct values of  $\gamma_b$  when  $\textit{We}_b = 0.05$ ,  $\textit{m}_a = 0.5$ ,  $\Sigma_b = 0.10$ ,  $\textit{A}_b^* = \textit{B}_b^* = -0.3$ ,  $\textit{R}_{ad} = 0.05$ , Pr = 6.2 and  $\textit{Bi}_b = 1.1$ .

 $\Gamma_a$  Time constant

 $\varphi$  Solid nanoparticles volume fraction

 $\sigma$  Electric conductivity

v Kinematic viscosity (m<sup>2</sup>/s)

 $\xi$  Pseudo-similarity variable

#### Acronyms

3D Three-Dimensional

Cu Copper Al<sub>2</sub>O<sub>3</sub> Alumina

PDEs Partial differential equations
ODEs Ordinary differential equations

BC Boundary conditions

SS Shear stress HTR heat transfer rate

#### Subscripts

hnf Hybrid nanofluidf Base fluid

w Condition at the wall surface

∞ Ambient condition

#### Superscript

Differentiation with respect to  $\xi$ 

#### Data availability

No data was used for the research described in the article.

#### References

- [1] S.U.S. Choi, Enhancing thermal conductivity of fluids with nanoparticles, Proceedings of the ASME International Mechanical Engineering Congress and Exposition 66 (1995) 99–105.
- [2] B. Xiao, W. Wang, X. Zhang, G. Long, J. Fan, H. Chen, L. Deng, A novel fractal solution for permeability and Kozeny-Carman constant of fibrous porous media made up of solid particles and porous fibers, Powder Technol. 349 (2019) 92, 88.
- [3] M. Liang, C. Fu, B. Xiao, L. Luo, Z. Wang, A fractal study for the effective electrolyte diffusion through charged porous media, Int. J. Heat Mass Tran. 137 (2019) 365–371.
- [4] R. Ekiciler, Effects of novel hybrid nanofluid (TiO<sub>2</sub>–Cu/EG) and geometrical parameters of triangular rib mounted in a duct on heat transfer and flow characteristics, J. Therm. Anal. Calorim. 143 (2021) 1371–1387.

- [5] L.S. Sundar, E.V. Ramana, Z. Said, A.M.B. Pereira, A.C.M. Sousa, Heat transfer of rGO/Co<sub>3</sub>O<sub>4</sub> hybrid nanomaterials-based nanofluids and twisted tape configuration in a tube, J. Therm. Sci. Eng. Appl. 13 (3) (2021) 031004.
- [6] H. Masuda, A. Ebata, K. Teramae, N. Hishinuma, Alteration of thermal conductivity and viscosity of liquid by dispersing ultra-fine particles, Netsu Bussei 7 (4) (1993) 227–233.
- [7] S.U.S. Choi, J.A. Eastman, The Proceedings of the 1995 ASME International Mechanical Engineering Congress and Exposition, vol. 245, ASME, San Francisco, USA, 1995, p. 99. FED 231/MD 66.
- [8] O.A. Bég, A.Y. Bakier, V.R. Prasad, Numerical modelling of non-similar mixed convection heat and species transfer along an inclined solar energy collector surface with cross diffusion effects, World J. Mech. 4 (1) (2011) 185–196.
- [9] N. Anbuchezhian, K. Srinivasan, K. Chandrasekaran, R. Kandasamy, Thermophoresis and Brownian motion effects on boundary layer flow of nanofluid in presence of thermal stratification due to solar energy, Appl. Math. Mech. English Ed. 33 (2012) 765–780.
- [10] J.A. Khan, M. Mustafa, T. Hayat, A. Alsaedi, Numerical study of Cattaneo-Christov heat flux model for viscoelastic flow due to an exponentially stretching surface, PLoS One 10 (9) (2015) e0137363.
- [11] A. Zeeshan, A. Majeed, Non Darcy mixed convection flow of magnetic fluid over a permeable stretching sheet with ohmic dissipation, J. Magnetics 21 (2016) 153–158.
- [12] M.D. Shamshuddin, F. Shahzad, W. Jamshed, O.A. Bég, M.R. Eid, T.A. Bég, Thermo-solutal stratification and chemical reaction effects on radiative magnetized nanofluid flow along an exponentially stretching sensor plate: computational analysis, J. Magnetism Mag. Mater. 565 (2023) 170286.
- [13] M.D. Shamshuddin, S.O. Salawu, K.K. Asogwa, P.S. Rao, Thermal exploration of convective transportation of ethylene glycol based magnetized nanofluid flow in porous cylindrical annulus utilizing MOS<sub>2</sub> and Fe<sub>3</sub>O<sub>4</sub> nanoparticles with inconstant viscosity, J. Magnetism Mag. Mater. 573 (2023) 170663.
- [14] S.P.A. Devi, S.S.U. Devi, Numerical investigation of hydromagnetic hybrid Cu -Al<sub>2</sub>O<sub>3</sub>/water nanofluid flow over a permeable stretching sheet with suction, Int. J. Nonlinear Sci. Numer. Stimul. 17 (2016) 249–257.
- [15] S.P.A. Devi, S.S.U. Devi, Heat transfer enhancement of Cu-Al<sub>2</sub>O<sub>3</sub>/water hybrid nanofluid flow over a stretching sheet, J. Niger. Math. Soc. 36 (2017) 419–433.
- [16] I. Waini, A. Ishak, I. Pop, Hybrid nanofluid flow and heat transfer past a permeable stretching/shrinking surface with a convective boundary condition, J. Phys.: Conf. Ser. 1366 (2019) 012022.
- [17] S. Salehi, A. Nori, Kh Hosseinzadeh, D.D. Ganji, Hydrothermal analysis of MHD squeezing mixture fluid suspended by hybrid nanoparticles between two parallel plates, Case Stud. Therm. Eng. 21 (2020) 100650.
- [18] Kh Hosseinzadeh, R. So, A. Asadi, A. Mogharrebi, D.D. Ganji, Investigation of micropolar hybrid ferrofluid flow over a vertical plate by considering various base fluid and nanoparticle shape factor, Int. J. Numer. Methods Heat Fluid Flow 31 (1) (2021) 402–417.
- [19] R.J.P. Gowda, R.N. Kumar, A. Aldalbahi, B.C. Prasannakumara, M. Rahimi-Gorji, M. Rahaman, Thermophoretic particle deposition in time-dependent flow of hybrid nanofluid over rotating and vertically upward/downward moving disk, J. Mol. Liq. 22 (2021) 100864.
- [20] F. Shahzad, W. Jamsheed, M.R. Eid, R.W. Ibrahim, R. Safdar, K.S. Nisar, Thermal amelioration in heat transfer rate using Oldroyd-B model hybrid nanofluid by CNTs-based kerosene oil flow in solar collectors applications, Waves Rand. Comp. Med.,.
- [21] I.L. Animasaun, Se-Jin Yook, T. Muhammad, A. Mathew, Dynamics of ternary-hybrid nanofluid subject to magnetic flux density and heat source or sink on a convectively heated surface, Surface. Interfac. 28 (2022) 101654.
- [22] M.D. Shamshuddin, O.A. Bég, N. Akkurt, H.J. Leonard, T.A. Bég, Analysis of unsteady thermo-solutal MoS<sub>2</sub>-EO Brinkman electro-conductive reactive nanofluid transport in a hybrid rotating Hall MHD generator, Partial Diff. Eq. Appl. Math. 7 (2023) 100525.
- [23] M.D. Shamshuddin, A. Saeed, K.K. Asogwa, Usman, W. Jamshed, A semi-analytical approach to investigate the entropy generation in a tangent hyperbolic magnetized hybrid nanofluid flow upon a stretchable rotating disk, J. Magnetism Mag. Mater. 574 (2023) 170644.
- [24] M.D. Shamshuddin, K.K. Asogwa, M. Ferdows, Thermo-solutal migrating heat producing and radiative Casson nanofluid flow via bidirectional stretching surface in the presence of bilateral reactions, Numer. Heat Tran. Part A: Appl. 85 (5) (2024) 719–738.
- [25] R.V. Williamson, The flow of pseudoplastic materials, Ind. Eng. Chem. 21 (11) (1929) 1108-1111.
- [26] S. Nadeem, S.T. Hussain, C. Lee, Flow of a Williamson fluid over a stretching sheet, Braz. J. Chem. Eng. 30 (3) (2013) 619-625.
- [27] T. Hayat, A. Shafiq, A. Alsaedi, Hydromagnetic boundary layer flow of Williamson fluid in the presence of thermal radiation and Ohmic dissipation, Alex. Eng. J. 55 (3) (2016) 2229–2240.
- [28] H.M. Shawky, N.T. Eldabe, K.A. Kamel, E.A. Abd-Aziz, MHD flow with heat and mass transfer of Williamson nanofluid over stretching sheet through porous medium, Microsyst. Technol. 25 (4) (2018) 1155–1169.
- [29] A.U. Yahya, N. Salamat, W.-H. Huang, I. Siddique, S. Abdal, S. Hussain, Thermal characteristics for the flow of Williamson hybrid nanofluid (MoS<sub>2</sub> + ZnO) based with engine oil over a stretched sheet, Case Stud, Therm. Eng. 26 (2021) 101196.
- [30] S.M. Hussain, Dynamics of radiative Williamson hybrid nanofluid with entropy generation: significance in solar aircraft, Sci. Rep. 12 (2022) 8916.
- [31] N. Ramachandran, T.S. Chen, B.F. Armaly, Mixed convection in stagnation flows adjacent to vertical surfaces, ASME J. Heat Transf. 110 (1988) 373-377.
- [32] C.D. Devi, H.S. Takhar, G. Nath, Unsteady mixed convection flow in stagnation region adjacent to a vertical surface, Heat Mass Tran. 26 (1991) 71–79.
- [33] A. Ishak, R. Nazar, N.M. Arifin, I. Pop, Dual solutions in mixed convection flow near a stagnation point on a vertical porous plate, Int. J. Therm. Sci. 47 (2008) 417–422.
- [34] U. Ahmad, M. Ashraf, A. Abbas, A.M. Rashad, H.A. Nabwey, Mixed convection flow along a curved surface in the presence of exothermic catalytic chemical reaction, Sci. Rep. 11 (2021) 12907.
- [35] H. Alfven, Discovery of alfven waves, Nature 150 (1942) 405.
- [36] T.G. Cowling, Magnetohydrodynamics, Wiley Inter Science, New York, 1957.
- [37] K.V. Prasad, K. Vajravelu, H. Vaidya, Hall effect on MHD flow and heat transfer over a stretching sheet with variable thickness, Int. J. Comput. Methods Eng. Sci. Mech. 17 (4) (2016) 288–297.
- [38] S. Gandluru, P.D.R.V. Rao, O.D. Makinde, Hydromagnetic-oscillatory flow of a nanofluid with Hall effect and thermal radiation past vertical plate in a rotating porous medium, Multidiscip. Model. Mater. Struct. 14 (2) (2018) 360–386.
- [39] F. Mabood, W.A. Khan, O.D. Makinde, Hydromagnetic flow of a variable viscosity nanofluid in a rotating permeable channel with Hall effects, J. Eng. Thermophys. 26 (2017) 553–566.
- [40] M. Veerakrishna, A.J. Chamkha, Hall effects on unsteady MHD flow of second grade fluid through porous medium with ramped wall temperature and ramped surface concentration, Phys. Fluids 30 (2018) 053101.
- [41] I. Tlili, N.N. Hamadneh, W.A. Khan, S. Atawneh, Thermodynamic analysis of MHD Couette–Poiseuille flow of water based nanofluids in a rotating channel with radiation and Hall effects, J. Therm. Anal. Calorim. 132 (2018) 1899–1912.
- [42] F.M. Abbasi, M. Gul, S.A. Shehzad, Hall effects on peristalsis of boron nitride-ethylene glycol nanofluid with temperature dependent thermal conductivity, Phys. E Low-dimens. Syst. Nanostruct. 99 (2018) 275–284.
- [43] N. Acharya, R. Raju Bag, P.K. Kundu, Influence of Hall current on radiative nanofluid flow over a spinning disk: a hybrid approach, Phys. E Low-dimens. Syst. Nanostruct. 111 (2019) 103–112.
- [44] M.S. Sundar, M.D. Shamshuddin, K. Spandana, Numerical simulation of stagnation point flow in magneto micropolar fluid over a stretchable surface under influence of activation energy and bilateral reaction, Int. Commun. Heat Mass Tran. 129 (2021) 105679.
- [45] M.S. Sundar, K. Spandana, M.D. Shamshuddin, S.O. Salawu, Mixed convective heat and mass transfer in magnetized micropolar fluid flow toward stagnation point on a porous stretching sheet with heat source/sink and variable species reaction, Int. J. Model. Simulat. 43 (5) (2023) 670–682.
- [46] E.M. Abo-Eldahab, M.A. El Aziz, Hall and Ion-Slip effects on MHD free convective heat generating flow past a semi-infinite vertical flat plate, Phys. Scripta A 61 (2000) 344.
- [47] G.W. Sutton, A. Sherman, Engineering Magnetohydrodynamics, McGraw-Hill, New York, 1965.
- [48] A. Zaib, S. Shafie, Thermal diffusion and diffusion thermo effects on unsteady MHD free convection flow over a stretching surface considering Joule heating and viscous dissipation with thermal stratification, chemical reaction and hall current, J. Franklin Inst. 351 (2014) 1268–1287.

- [49] D. Pal, G. Mandal, Influence of Lorentz force and thermal radiation on heat transfer of nanofluids over a stretching sheet with velocity-thermal slip, Int. J. Appl. Comput. Math. 3 (2017) 3001–3020.
- [50] B. Takabi, S. Salehi, Augmentation of the heat transfer performance of a sinusoidal corrugated enclosure by employing hybrid nanofluid, Adv. Mech. Eng. 2014 (2014) 147059.
- [51] A. Mahdy, Unsteady mixed convection boundary layer flow and heat transfer of nanofluids due to stretching sheet, Nucl. Eng. Des. 249 (2012) 248–255. [52] J.H. Merkin, On dual solutions occurring in mixed convection in a porous medium, J. Eng. Math. 20 (2) (1986) 171–179.
- [53] P.D. Weidman, D.G. Kubitschek, A.M.J. Davis, The effect of transpiration on self-similar boundary layer flow over moving surfaces, Int. J. Eng. Sci. 44 (11/12)
- [54] S.D. Harris, D.B. Ingham, I. Pop, Mixed convection boundary-layer flow near the stagnation point on a vertical surface in a porous medium: brinkman model with slip, Transport Porous Media 77 (2) (2009) 267–285.
- [55] A. Ishak, R. Nazar, I. Pop, Hydromagnetic flow and heat transfer adjacent to a stretching vertical sheet, Heat Mass Tran. 44 (2008) 921–927.